

Experimental partitioning of halogens and other trace elements between olivine, pyroxenes, amphibole and aqueous fluid at 2 GPa and 900–1,300 °C

Alessandro Fabbrizio · Roland Stalder ·
Kathrin Hametner · Detlef Günther ·
Katharina Marquardt

Received: 11 March 2013 / Accepted: 31 May 2013 / Published online: 19 June 2013
© The Author(s) 2013. This article is published with open access at Springerlink.com

Abstract We present new partition coefficients for various trace elements including Cl between olivine, pyroxenes, amphibole and coexisting chlorine-bearing aqueous fluid in a series of high-pressure experiments at 2 GPa between 900 and 1,300 °C in natural and synthetic systems. Diamond aggregates were added to the experimental capsule set-up in order to separate the fluid from the solid residue and enable in situ analysis of the quenched solute by LA-ICP-MS. The chlorine and fluorine contents in mantle minerals were measured by electron microprobe, and the nature of OH defects was investigated by infrared spectroscopy. Furthermore, a fluorine-rich olivine from one selected sample was investigated by TEM. Results reveal average Cl concentrations in olivine and pyroxenes around 20 ppm and up to 900 ppm F in olivine, making olivine an important repository of halogens in the mantle. Chlorine is always incompatible with Cl partition coefficients $D_{\text{Cl}}^{\text{olivine/fluid}}$ varying between 10^{-5} and 10^{-3} , whereas $D_{\text{Cl}}^{\text{orthopyroxene/fluid}}$ and $D_{\text{Cl}}^{\text{clinopyroxene/fluid}}$ are $\sim 10^{-4}$ and $D_{\text{Cl}}^{\text{amphibole/fluid}}$ is

$\sim 5 \times 10^{-3}$. Furthermore, partitioning results for incompatible trace element show that compatibilities of trace elements are generally ordered as $D^{\text{amph/fluid}} \approx D^{\text{cpx/fluid}} > D^{\text{opx/fluid}} > D^{\text{ol/fluid}}$ but that $D^{\text{mineral/fluid}}$ for Li and P is very similar for all observed silicate phases. Infrared spectra of olivine synthesized in a F-free Ti-bearing system show absorption bands at 3,525 and $\sim 3,570 \text{ cm}^{-1}$. In F \pm TiO₂-bearing systems, additional absorption bands appear at $\sim 3,535$, $\sim 3,595$, 3,640 and $3,670 \text{ cm}^{-1}$. Absorption bands at $\sim 3,530$ and $\sim 3,570 \text{ cm}^{-1}$, previously assigned to humite-like point defects, profit from low synthesis temperatures and the presence of F. The presence of planar defects could not be proved by TEM investigations, but dislocations in the olivine lattice were observed and are suggested to be an important site for halogen incorporation in olivine.

Keywords Halogens · Trace element partitioning · Mantle · Defects · TEM

Communicated by J. Hoefs.

Electronic supplementary material The online version of this article (doi:10.1007/s00410-013-0902-5) contains supplementary material, which is available to authorized users.

A. Fabbrizio (✉) · R. Stalder
Institute of Mineralogy and Petrography, University
of Innsbruck, Innrain 52f, 6020 Innsbruck, Austria
e-mail: Alessandro.Fabbrizio@uibk.ac.at

K. Hametner · D. Günther
Lab of Inorganic Chemistry, ETH Zürich, Wolfgang-Pauli-Str.
10, 8093 Zurich, Switzerland

K. Marquardt
Deutsches GeoForschungsZentrum, Section 3.3, Telegrafenberg,
14473 Potsdam, Germany

Introduction

Mantle minerals such as olivine, ortho- and clinopyroxene can host up to several hundreds ppm water (Rauch and Keppler 2002; Hirschmann et al. 2005; Stalder et al. 2005, 2008; Grant et al. 2007a; Tenner et al. 2009). The incorporation mechanism of OH in mantle minerals is important for understanding the rheology, partial melting, diffusion, electrical conductivity, seismic wave speeds and attenuation of the mantle and has been studied intensely in the previous decades (e.g., Bell and Rossman 1992; Hirth and Kohlstedt 1996; Karato and Jung 1998). In contrast, the role of the halogens F and Cl in the mantle is not well investigated. From geochemical considerations (Cl/K and

F/P ratios of melt inclusions from mid-ocean ridge basalts and the estimated K and P contents of the upper mantle), the abundance of chlorine in the mantle is estimated to approximately 1 ppm and that of fluorine to 16 ppm (Saal et al. 2002). Despite their low abundances in the mantle, halogens exert a significant role on the genesis and evolution of magmas. Halogens play an important role in volcanic and related magmatic systems (Aiuppa et al. 2009; Baker and Balcone-Boissard 2009; Webster et al. 2009). Halogens are separated from magma in the Earth's crust during cooling and crystallization (Carroll and Webster 1994) and exert significant impact on the genesis of hydrothermal systems (e.g., Reed 1997) and on the transport of ore-forming metals (Yardley 2005; Vigneresse 2009).

Halogen solubilities in nominally anhydrous mantle minerals at mantle conditions are scarcely documented, but seem to be much higher than observed in natural samples (Beyer et al. 2012). Experimental results in the system $\text{Mg}_2\text{SiO}_4\text{--MgF}_2$ (Bromiley and Kohn 2007) reveal up to 0.45 wt% F in forsterite, but no apparent correlation between F and Mg concentrations in the olivine could be established, and the incorporation mechanisms could not be solved. In contrast, Cl solubilities are much lower. Chlorine concentrations for forsterite and enstatite in fluid-bearing systems cluster around 3 ppm in the system forsterite–enstatite–pyrope– H_2O – MgCl_2 (Bernini et al. 2013). In contrast, Cl concentrations around 20 ppm were observed in the system $\text{MgO--SiO}_2\text{--H}_2\text{O} \pm \text{TiO}_2 \pm \text{Al}_2\text{O}_3$ under similar P – T conditions (Fabrizio et al. 2013), where the enhanced Cl solubilities in forsterite in the presence of TiO_2 suggest a Cl incorporation in forsterite via the stabilization of defects that are stabilized by Ti, e.g., humite-type defects. Ti plays an important role in the formation of hydroxyl point defects in olivine associated with trace Ti substitutions (Berry et al. 2005), and planar humite type associated with Ti has been detected in olivine from different localities (Kitamura et al. 1987; Drury 1991; Risold et al. 2001; Hermann et al. 2007) by transmission electron microscopy (TEM). Both kinds of defects are able to host halogens that substitute some of the OH. In addition to planar and point defects, the growth of nanometer-sized Ti-clinohumite nuclei during hydrous alteration in olivine at 8 GPa and 1,300 K has been described (Wirth et al. 2001), otherwise no detailed TEM studies have been carried out to confirm the presence of humite-type defects in synthetic olivine. Olivine crystals that have been investigated by TEM and revealed humite-type planar defects exhibit IR absorption bands at 3,564 and 3,394 cm^{-1} , identical in energy to absorption bands in Ti-clinohumite (Hermann et al. 2007). In contrast, Ti-related OH point defects in olivine cause IR absorption bands at 3,525 and 3,572 cm^{-1} (Berry et al. 2005). Partitioning experiments at

upper mantle conditions between nominally halogen-free minerals and coexisting basaltic melts both in natural and in synthetic systems show that (1) F and Cl are always incompatible in mantle minerals, (2) the compatibilities are generally ordered as $D^{\text{Cpx/melt}} > D^{\text{Opx/melt}} > D^{\text{Grt/melt}} > D^{\text{Ol/melt}} > D^{\text{Plag/melt}}$ and (3) F is less incompatible than Cl (Beyer et al. 2012; Dalou et al. 2012).

In this study, we present new experimental results derived from synthesis experiments at 2 GPa and 900–1,300 °C for F and Cl incorporation in olivine, ortho-, clinopyroxene, and amphibole and mineral/fluid partition coefficient for Cl in the system $\text{MgO--SiO}_2\text{--H}_2\text{O} \pm \text{TiO}_2 \pm \text{NaCl} \pm \text{MgF}_2 \pm \text{CaF}_2$ and in natural composition doped with TiO_2 , NaCl or CaF_2 . A combination of electron microprobe and LA–ICP–MS was used to analyze Cl in the resulting phases. The quality and quantity of OH defects in olivine were characterized by IR spectroscopy, and transmission electron microscopy (TEM) was used to investigate the relations between the OH-related IR absorption bands and humite-type defects.

Experimental and analytical methods

Starting materials and sample preparation

The starting materials for the experimental runs consisted of a natural peridotite from Stöppling/Germany (details concerning petrography see Oehm et al. 1983; composition was determined by XRF: $\text{SiO}_2 = 44.2$ wt%; $\text{Al}_2\text{O}_3 = 1.3$ wt%; $\text{Fe}_2\text{O}_3 = 9.4$ wt%; $\text{MnO} = 0.1$ wt%; $\text{MgO} = 43.6$ wt%; $\text{CaO} = 1.3$ wt%) and of a synthetic MSH ($\text{MgO} = 40.3$ wt%; $\text{SiO}_2 = 41.7$ wt%; $\text{H}_2\text{O} = 18$ wt%) powder both doped with TiO_2 , NaCl, CaF_2 or MgF_2 (Table 1).

Starting mixtures were prepared by grounding the peridotite and the synthetic $\text{Mg}(\text{OH})_2\text{--SiO}_2$ mixture in an agate mortar under ethanol for 1 h and subsequently in an automatic milling machine for 1 h. The doping agents were then added to the starting mixtures in the desired amount. In addition, barium was added as BaTiO_3 to the peridotite mixture. Barium is highly incompatible in mantle minerals. Therefore, it resides preferably in the fluid or melt phase and can be used as internal standard for quantification of LA–ICP–MS analyses. The doped starting mixtures were ground again in the agate mortar under ethanol for 1 h to achieve chemical homogeneity.

As sample containers, we used Pt capsules with an outer (inner) diameter of 3.0 (2.6) mm. For experiments with the diamond trap, a Pt ring with an inner diameter of 2.1 mm and a height of 1 mm was inserted into the Pt capsule. Then, ~ 6 μl H_2O was added to the capsule, corresponding to 15 wt% of the starting powder + water mixture. The capsule was then filled with 6–7 mg of synthetic diamond

Table 1 Starting mixtures, experimental conditions^a and phase relations of the run products

Run	Starting material	<i>T</i> (°C)	Time (h)	Run products identified
Cl-22	Peridotite + 0.3 % TiO ₂ + 22 % NaCl	1,300	24	ol, salt, fluid
Cl-23	Peridotite + 0.3 % TiO ₂ + 22 % NaCl	1,200	48	ol, salt, fluid
Cl-24	Peridotite + 0.3 % TiO ₂ + 22 % NaCl	1,100	72	ol, opx, salt, fluid
Cl-25	Peridotite + 0.3 % TiO ₂ + 22 % NaCl	1,000	96	ol, opx, cpx, salt, fluid
Cl-26	Peridotite + 0.3 % TiO ₂ + 22 % NaCl	900	144	ol, opx, cpx, amph, salt, fluid
Cl-22 ^b	Peridotite + 0.3 % TiO ₂ + 22 % NaCl	1,300	24	ol, salt, fluid
Cl-23 ^b	Peridotite + 0.3 % TiO ₂ + 22 % NaCl	1,200	48	ol, salt, fluid
Cl-24 ^b	Peridotite + 0.3 % TiO ₂ + 22 % NaCl	1,100	72	ol, opx, salt, fluid
Cl-25 ^b	Peridotite + 0.3 % TiO ₂ + 22 % NaCl	1,000	96	ol, opx, cpx, salt, fluid
Cl-26 ^b	Peridotite + 0.3 % TiO ₂ + 22 % NaCl	900	144	ol, opx, cpx, amph, salt, fluid
F-2	MSH + 0.3 % TiO ₂ + 1 % CaF ₂	1,300	24	fo, en, salt, fluid
F-3	MSH + 0.3 % TiO ₂ + 1 % CaF ₂	1,200	48	fo, chu, en, salt, fluid
Cl-F-1	MSH + 22 % NaCl + 2 % MgF ₂	1,200	48	fo, en, salt, fluid
F-1	MSH + 0.3 % TiO ₂ + 1 % CaF ₂	1,000	96	fo, en, di, tr, tlc ^d , salt, fluid
F-5 ^c	Peridotite + 0.3 % TiO ₂ + 22 % NaCl + 2 % CaF ₂	1,300	24	ol, sp, salt, fluid
F-4 ^c	Peridotite + 0.3 % TiO ₂ + 22 % NaCl + 2 % CaF ₂	1,300	24	ol, salt, fluid
F-6	Peridotite + 0.3 % TiO ₂ + 22 % NaCl + 2 % CaF ₂	1,300	24	ol, opx, salt, fluid
F-7	Peridotite + 0.3 % TiO ₂ + 22 % NaCl + 2 % CaF ₂	1,100	72	ol, opx, salt, fluid

Ol olivine, *opx* orthopyroxene, *cpx* clinopyroxene, *amph* amphibole, *fo* forsterite, *en* enstatite, *chu* clinohumite, *di* diopside, *tlc* talc, *tr* tremolite, *sp* spinel

^a All runs were performed at a pressure of 2 GPa

^b Experiment performed with diamond trap

^c Capsule lined with Ni (F-4) and Fe (F-5) foil

^d Supposed by mixed analysis fo + tlc (Table 3)

crystals (grain size 20 μm) kindly provided by Servisix GmbH (Karlstein, Germany) and with 35–55 mg of the starting material powder. For experiments without the diamond trap, the set-up of the capsule was the same except for the Pt ring and for the diamond crystals that were not used. For experiments with the MSH mixtures, 2 μl H₂O was added to the capsule. The capsule was welded while cooled in water, and the weight of the capsule was compared before and after welding to ensure that no water was lost during welding. The sealed capsule was squeezed to a final cylindrical shape with a length of 5.5–6.5 mm and then held at 120 °C for 24 h, in order to check whether the capsule was sealed properly.

Experiments

Experiments were carried out in an end-loaded piston-cylinder apparatus at 2 GPa and temperatures in the range of 900–1,300 °C for durations between 1 and 6 days at Innsbruck University (Table 1). The concentric cylindrical high-pressure assemblies consist (from outside to inside) of a lead foil wrapped around a talc cell, a Pyrex cylinder, a graphite furnace and inner pieces of crushable alumina

sleeves. In two experiments, the interior walls of the capsules were lined with Ni (run F-4) and Fe foil (run F-5) to control the *f*O₂ (Table 1). At pressure and temperature of interest (2.0 GPa and 1,300 °C), the calculated log*f*O₂ for the controlling reaction Fe–FeO is ~3 log units below the QFM buffer (QFM-3) and for the reaction Ni–NiO is ~1.5 log units above the QFM buffer (QFM + 1.5) (O'Neill 1988; O'Neill and Pownceby 1993). Run temperatures were controlled within ~1 °C of the set point using Pt/Pt₉₀Rh₁₀ thermocouples accurate to within ±3 °C. The range in temperature across the length of the capsules during the experiments is estimated to be less than 20 °C. The experimental charge is placed in the hotspot of the experimental assembly to prevent unwanted crystal growth within the diamond trap (Aerts et al. 2010). No pressure correction was applied to the EMF. The power output was monitored during the entire duration of all runs in order to ensure that no temperature drift occurred. Each experiment was initiated by gently increasing the sample pressure to approximately 0.25 GPa followed by a heating to 1,400 °C at a rate of 15 °C/min and a simultaneous pressure increase until the final pressure was reached. To grow relatively large, high-quality crystals necessary for IR spectroscopy,

synthesis experiments were heated to 1,400 °C and then slowly cooled to final temperature at a rate of 6 °C/h. Depending on the temperature, the experimental run time was in the range 24–144 h (Table 1), corresponding to the time needed to achieve equilibrium in similar systems under similar conditions (Stalder et al. 2001; Stalder and Ulmer 2001; Fabbriozio et al. 2013). All runs were terminated by switching off the power. After decompression, the charge was removed from the assembly, and the recovered capsule was weighed and pierced to check for potential leakage. When pierced, the pH of the extruding fluid was checked with indicator paper; the checked fluid was in all cases neutral (pH = 7), indicating that the possibly dissolved alkalis are balanced by chlorine, that Al acidic and basic species are negligible and that neutral complex such as $\text{NaAl}(\text{OH})_4$ may form. Subsequently, the pierced capsule was dried in an oven at 120 °C (upon drying, salt crystals formed at the opening of the capsule) and weighed again. Usually, the weight loss upon drying corresponds to 90–100 % of the initial water content. In the two samples buffered by the reactions Fe–FeO and Ni–NiO, remnant metal foil from the oxygen buffer material and brightly colored crystalline material was recovered from the capsule. The metal foil was analyzed by EDS during the EMPA session. All recovered capsules were embedded in epoxy and ground by hand. As soon as the trap became visible, the sample was impregnated with epoxy to prevent destruction during preparation. Later, the capsule was ground until its maximum cross section was exposed.

Electron microprobe

Electron microprobe measurements were taken using a Jeol Superprobe 8100 at Innsbruck University. The crystals were analyzed with an electron beam energy of 15 keV, a beam current of 10 nA, a focused beam and counting times of 20 s. Subsequently, Ti, Na, Cl and F were measured with a beam current of 400 nA and 240-s counting time on peak and 120 s on the background. A detailed explanation of the analytical protocol to measure chlorine concentrations, including a comparison with samples for which the Cl contents were independently determined, is reported in Fabbriozio et al. (2013). Quartz (Si), diopside (Ca), olivine (Mg), rutile (Ti), aegirine (Na), atacamite (Cl), corundum (Al), chromite (Cr), almandine (Fe), rhodonite (Mn), Ni-olivine (Ni) and F-topaz (F) were used as standards. Replicate analyses were carried out on the same sample (30–40 points in each sample) to check for compositional homogeneity. Limits of detection were 2 ppm for Cl, 6 ppm for Na, 9 ppm for Ti and 15 ppm for F. Associated relative errors (based on counting statistics) were less than 10 % for Cl, less than 5 % for Na, ~20 % for Ti and less than 1 % for F. Due to the overlap of the $\text{Fe}L\alpha$ over the $\text{FK}\alpha$, fluorine was analyzed only in the Fe-free

experiments. The BSE images show the absence of fluid inclusions inside the crystals and the absence of beam damage on the surface of the crystals after the electron microprobe analysis for Cl (Fig. 1).

LA-ICP-MS

Element concentrations of the crystalline phases and of the fluid solute trapped between the diamonds were analyzed by LA-ICP-MS at the Laboratory for Inorganic Chemistry, ETH Zürich, using a 193-nm ArF excimer laser system (Günther et al. 1997) coupled to an ELAN 6100 quadrupole ICP-MS. All elements except Cl were standardized against a NIST SRM610 glass, and a synthetic Cl-bearing basaltic glass (Fabbriozio et al. 2013) was used as standard for Cl. The glass was analyzed two times before and two times after performing analyses of the samples of interest and served as external standard. Na was used as internal standard for the synthetic glass. Ba was used for internal standardization to calculate element concentration in the quenched fluid, by assuming that Ba (the most incompatible element in this study) partitions totally into the fluid phase.

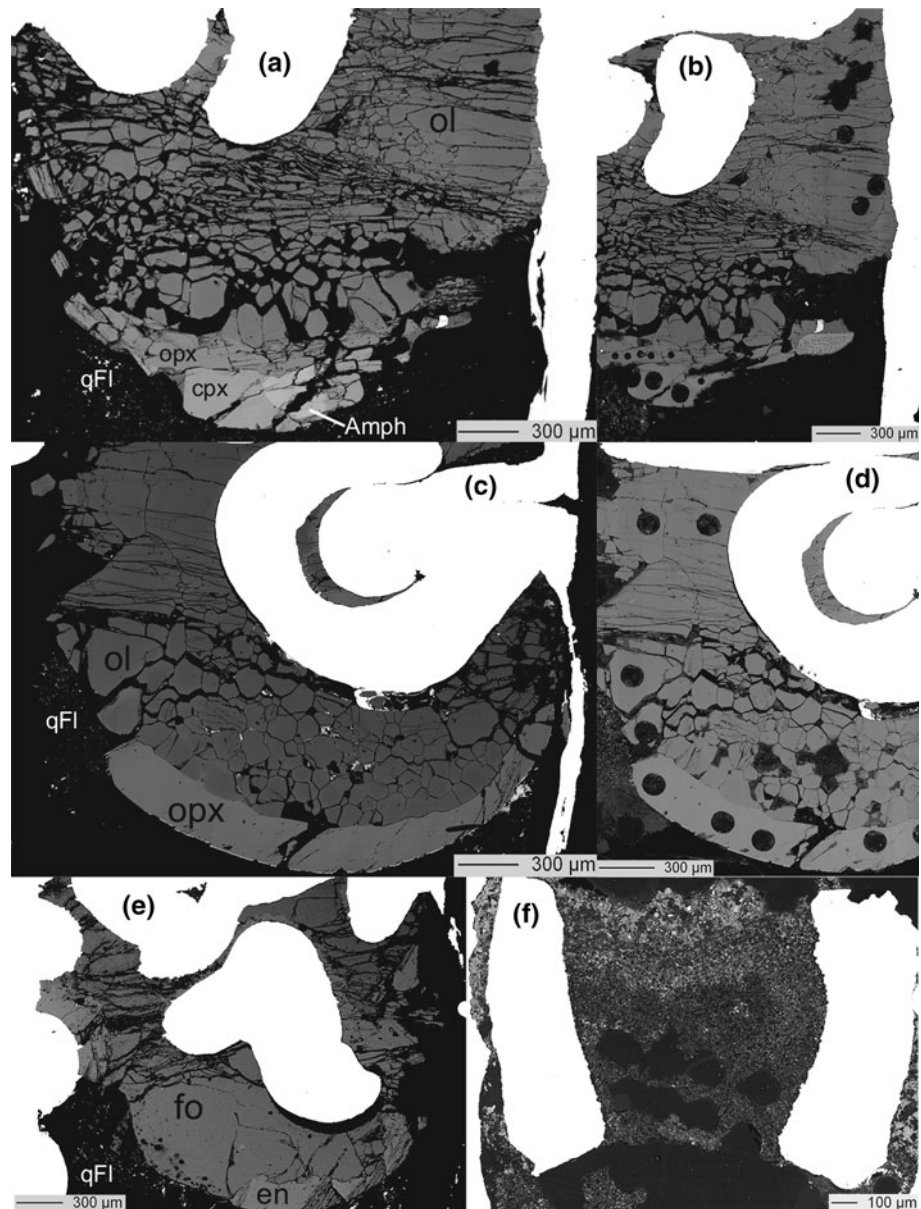
Diamond traps (Fig. 1f) were measured with the laser imaged to 120 μm diameter at repetition rates of 5 Hz. Eight analyses were carried out on the diamond trap for each sample. In order to check the potential influence of mass interferences of $^{23}\text{Na}^{12}\text{C}$ and ^{35}Cl , both chlorine isotopes (^{35}Cl and ^{37}Cl) were measured. Since the differences in the isotope ratio were always below 3 %, the influence of this interference was considered negligible. The detection limit for chlorine was below 100 ppm. For minerals analysis, the NIST SRM610 glass was used to calibrate elements. Element concentration calculations were based on the Si concentration as determined by electron microprobe analysis. For the analysis of the crystalline phases, the diameter of the laser was adjusted as function of the crystal size (Fig. 1b, d); in general, beam diameters of 50–120 μm were used at repetition rates of 5 Hz.

IR spectroscopy

All experimental charges were cut as whole capsule by a diamond wire saw to preserve the texture, and then, double-sided polished wafers of 150 μm thickness were prepared. Sample thicknesses were measured using a Mitutoyo micrometer and are accurate to $\pm 2 \mu\text{m}$. In order to evaluate the orientation of the measured olivine crystals, reference spectra on oriented olivine crystals from Stöppling/Germany (Oehm et al. 1983) were recorded that were later compared with the olivine spectra of the experimental charges (Fig. 2).

IR spectra were recorded at room temperature in transmission mode using a Bruker Vertex 70 FTIR

Fig. 1 BSE images of **a** sample CI-26, **b** sample CI-26 with laser ablation spots in the crystalline phases, **c** sample CI-24, **d** sample CI-24 with laser ablation spots in the crystalline phases, **e** sample CI-F-1, the one investigated by TEM, **f** diamond trap of sample CI-22 after laser ablation analysis. The *circular holes* are laser ablation pits now filled by epoxy. *Ol* olivine (dark gray), *opx* orthopyroxene (medium gray), *cpx* clinopyroxene (light gray), *amph* amphibole (lighter gray), *en* enstatite (light gray), *fo* forsterite (dark gray), *qFl* quenched fluid



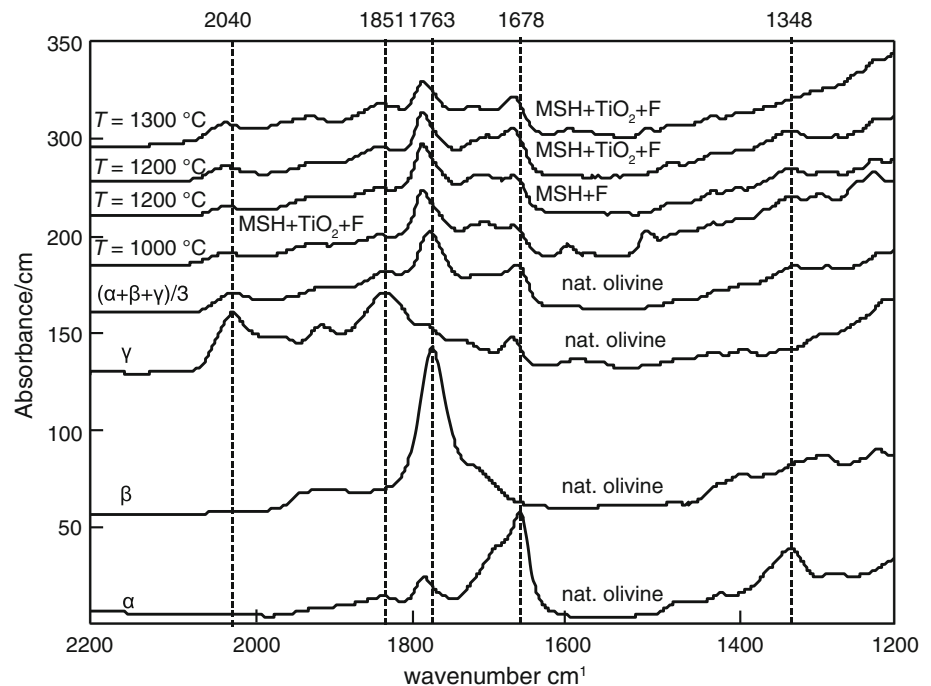
spectrometer, which was continuously flushed with dried air to minimize water–vapor background, coupled to a Hyperion 3000 microscope equipped with (1) a usual nitrogen-cooled MCT-D316-025 (mercury cadmium telluride) detector (in the following called single-element detector) and (2) a nitrogen-cooled focal plane array (FPA) detector consisting of 64×64 MCT-D364 detectors. For measurements with the single-element detector, each spectrum was acquired by 64 scans in the $550\text{--}7,500\text{ cm}^{-1}$ range with a spectral resolution of 2 cm^{-1} . The FPA detector enables FTIR imaging of an area measuring $170 \times 170\text{ }\mu\text{m}$ with a lateral pixel resolution of $2.7\text{ }\mu\text{m}$. For each spectrum, 64 scans in the $850\text{--}3,950\text{ cm}^{-1}$ range were acquired with a spectral resolution of 4 cm^{-1} . Selected spectral ranges were

integrated automatically for all spectra, and the results were color-coded and graphically displayed as a map that was used as overview for measurements with the IR single-element detector masked with apertures of typically $50 \times 50\text{ }\mu\text{m}^2$. Grain boundaries and areas on the crystal, which are penetrated by cracks or inclusions, could be easily detected and avoided as analysis area for IR measurements. From each capsule and on each wafer, unpolarized spectra of 10–15 randomly oriented olivine single crystals were recorded and averaged.

TEM

In order to check whether F in olivine is incorporated by F-clinochomite lamellae (Stalder and Ulmer 2001),

Fig. 2 Polarized IR spectra of olivine sections parallel to α , β , γ and average spectrum $(\alpha + \beta + \gamma)/3$. Unpolarized IR spectra of olivine averaged over 10–15 randomly oriented crystals from the MSH + F \pm TiO₂ system



transmission electron microscopy (TEM) was carried out on a forsterite of run Cl-F-1 using a FEI Tecnai G² F²⁰ X-Twin transmission electron microscope at GeoForschungsZentrum Potsdam, Germany, operated at 200 kV. Selected area electron diffraction (SAED), combined with bright field (BF), high-resolution (HR-TEM) and scanning transmission electron microscopy using a high-angle annular dark field detector in scanning transmission mode (STEM-HAADF), was performed to investigate the local defect structure of forsterite. The sample for TEM was prepared by first determining the orientation of the olivine using electron-backscattered diffraction (EBSD) with an Ultra 55 Plus (Carl Zeiss SMT) field emission scanning electron microscope. The foil for TEM was prepared by the focused ion beam technique (FIB) (Wirth 2004; Lee et al. 2003; Phaneuf 1999) using a FEI FIB200TEM focused ion beam device. After cutting the foil to the dimensions of $12 \times 8 \mu\text{m}^2$ and a thickness of about 100 nm, the foil was extracted from the excavation site using the lift-out technique (Giannuzzi et al. 1997). It was transferred to a copper TEM grid with a holey carbon foil to sustain the TEM foil using a manipulator.

Results

Textures of minerals and diamond traps

Experimental conditions and results are summarized in Tables 1, 2 and 3 and in the Online Resource 1. Since one

of the aims of this study was the determination of mineral/fluid partition coefficients, it is important to judge whether crystals grew subsolidus (and consequently the term ‘fluid’ can be used) or supersolidus, i.e., in the presence of a hydrous melt. The simple system forsterite–enstatite–water approaches melting at 1,400 °C and 2 GPa (Kushiro and Yoder 1969); however, the presence of NaCl suppresses melting because it lowers the water activity (Aranovich and Newton 1996, 1997; Shmulovich and Graham 1996). A Cl/(Cl + H₂O) molar ratio of 0.2 and 0.4 increases the temperature of the solidus in the system Mg₂SiO₄ + MgSiO₃ + H₂O + KCl at 5 GPa, respectively, of ~200 and ~350 °C (Chu et al. 2011). Consequently, since the experiments reported here have a Cl/(Cl + H₂O) molar ratio of 0.3, they can be considered being subsolidus. The textures of the experimental charges can serve as additional constraint of the absence of a melt during the runs. Textures of representative run products are shown in Fig. 1. No particular textural differences are noted between experiments performed at different temperatures (Fig. 1a–e). Phases interpreted to have crystallized in equilibrium with each other in the absence of a melt are euhedral to subhedral and typically have the same grain size. The quenched phase is subhedral and typically displays acicular habit. The small amount of quench phase (Fig. 1a–e) is interpreted to represent the solute quenched from the subsolidus fluid phase. No abrupt increase in the amount of quenched phase with temperature was observed, which is interpreted to indicate the absence of a melt in all performed experiments.

Phase assemblages

Run products were mainly composed of olivine, pyroxenes, salt and aqueous fluid. In single cases, additional phases such as clinohumite, amphibole or spinel were observed. Individual phase assemblages are listed in Table 1. The size of the crystals varied between 80 and 300 μm in the natural system and was over 300 μm in the MSH system (Fig. 1). Electron microprobe analyses are listed in the Online Resource 1 and in Table 2. No chemical zoning patterns were observed. In the experiments with the natural composition, only olivine (Fo_{97}) is present at temperature

above 1,100 $^{\circ}\text{C}$, at 1,100 $^{\circ}\text{C}$ orthopyroxene appears, at 1,000 $^{\circ}\text{C}$ olivine coexists with ortho- and clinopyroxene and at 900 $^{\circ}\text{C}$ amphibole occurred in addition. Spinel coexists with olivine in the run buffered by the reaction $\text{Fe}-\text{FeO}$. The Cl concentrations in olivine are 20 ± 14 ppm, in opx 26 ± 10 ppm and in cpx 20 ± 4 ppm, whereas the Cl contents of amphibole is 585 ± 36 ppm.

In the synthetic system, forsterite (Fo_{100}) coexists with enstatite in all runs. At 1,200 $^{\circ}\text{C}$, clinohumite coexists with forsterite and enstatite and at 1,000 $^{\circ}\text{C}$ F-tremolite (4.2 wt% F), diopside ($\text{Di}_{85}\text{En}_{15}$ containing 690 ppm F) and an unidentified F-bearing phase—supposedly talc—

Table 2 Analyses of the run products (model system and natural peridotite) by EMPA

Experiment (<i>P</i> , GPa/ <i>T</i> , $^{\circ}\text{C}$)	F-2 (2/1300)		F-3 (2/1200)			Cl-F-1 (2/1200)		F-1 (2/1000)			
	fo	en	fo	en	chu	fo	en	fo	en	fo+tlc	tr
SiO_2 (wt%)	43.20 (18)	60.58 (33)	40.75 (58)	58.99 (86)	36.66 (40)	42.95 (51)	58.72 (51)	42.44 (22)	59.84 (30)	49.63	59.10 (48)
TiO_2	0.0015 (5)	0.03 (0)	0.03 (0.01)	0.01 (1)	0.97 (10)	–	–	–	0.06 (2)	0.40	0.24 (5)
Al_2O_3	–	–	–	–	–	–	–	–	–	–	–
Cr_2O_3	–	–	–	–	–	–	–	–	–	–	–
FeO	–	–	–	–	–	–	–	–	–	–	–
MnO	–	–	–	–	–	–	–	–	–	–	–
MgO	55.34 (21)	38.47 (25)	59.20 (38)	41.31 (19)	57.27 (40)	55.71 (23)	38.56 (30)	57.96 (31)	40.47 (14)	47.52	27.36 (95)
NiO	–	–	–	–	–	–	–	–	–	–	–
CaO	0.03 (0)	0.18 (2)	0.02 (1)	0.29 (13)	0.00	–	–	0.02 (1)	0.23 (10)	0.26	10.79 (7)
Na_2O	–	–	–	–	–	0.03 (4)	0.06 (7)	–	–	–	–
Cl	–	–	–	–	–	0.017 (7)	0.003 (2)	–	–	–	–
F	0.00	0.00	0.077 (30)	0.00	3.06 (0.1)	0.090 (4)	0.00	0.00	0.00	3.14	2.04 (10)
Total	98.6 (3)	99.3 (4)	100.0 (9)	100.6 (9)	98.0 (5)	98.8 (5)	97.3 (5)	100.4 (3)	100.6 (4)	100.9	99.5 (5)
$D_{\text{Cl}}^{\text{mineral/startmix}}$						0.0016	0.00029				
$D_{\text{F}}^{\text{mineral/startmix}}$			0.16		6.25	0.096				6.41	4.16
Experiment (<i>P</i> , GPa/ <i>T</i> , $^{\circ}\text{C}$)	F-1 (2/1000) di	^a F-5 (2/1300) ol	ox	^b F-4 (2/1300) ol	F-6 (2/1300) ol	opx	F-7 (2/1100) ol	opx			
SiO_2 (wt%)	55.31 (14)	38.26 (44)	0.38 (3)	39.98 (23)	42.03 (13)	58.94 (31)	41.90 (13)	57.90 (24)			
TiO_2	0.21 (4)	0.023 (3)	0.99 (9)	0.0033 (11)	0.0037 (9)	0.07 (2)	0.0053 (15)	0.10 (1)			
Al_2O_3	–	0.09 (2)	1.24 (3)	0.01 (1)	0.00	0.38 (14)	0.00	0.52 (7)			
Cr_2O_3	–	0.07 (4)	1.99 (34)	0.13 (7)	0.09 (4)	0.34 (7)	0.04 (3)	0.46 (23)			
FeO	–	22.64 (93)	80.82 (57)	1.76 (38)	0.29 (5)	0.16 (6)	3.63 (24)	4.31 (7)			
MnO	–	0.07 (2)	0.06 (3)	0.11 (2)	0.07 (2)	0.06 (2)	0.07 (2)	0.11 (2)			
MgO	21.73 (37)	39.22 (79)	14.71 (16)	46.21 (22)	55.90 (32)	38.23 (5)	53.31 (19)	34.32 (25)			
NiO	–	0.02 (2)	0.12 (6)	12.07 (75)	0.06 (5)	0.03 (2)	0.32 (1)	0.13 (2)			
CaO	22.66 (48)	0.34 (3)	0.02 (1)	0.09 (1)	0.05 (2)	0.44 (2)	0.06 (2)	1.27 (12)			
Na_2O	–	0.02 (2)	0.10 (6)	0.04 (2)	0.05 (3)	0.13 (1)	0.04 (2)	0.20 (3)			
Cl	–	0.0014 (5)	na	0.0015 (5)	0.0015 (5)	0.0019 (7)	0.0056 (20)	0.0034 (7)			
F	0.069 (16)	na	na	na	na	na	na	na			
Total	100.0	100.7 (5)	100.4 (1)	100.4 (4)	98.6 (3)	98.8 (4)	99.39 (26)	99.33 (28)			
$D_{\text{Cl}}^{\text{mineral/startmix}}$		0.00013		0.00014		0.00018	0.00053	0.00032			
$D_{\text{F}}^{\text{mineral/startmix}}$	0.14										

^a Capsule lined with Fe foil

^b Capsule lined with Ni foil

Table 3 Mineral/fluid partition coefficients

Sample (P, GPa/T, °C)	2/1,200		2/1,100		2/1,000		2/900		cpx	opx	amph
	ol	opx	ol	opx	ol	opx	ol	opx			
Cl	9×10^{-5} (2)	1.8×10^{-5} (16)	2×10^{-4} (8)	1.7×10^{-4} (8)	1.8×10^{-4} (8)	3.7×10^{-4} (8)	2×10^{-4} (3)	1.5×10^{-4} (3)	1.4×10^{-4} (4)	1.5×10^{-4} (2)	0.0049 (3)
Li	0.13 (4)	0.07 (3)	0.33 (13)	0.31 (9)	0.27 (10)	0.18 (6)	0.25 (11)	0.35 (7)	0.48 (7)	0.72 (19)	0.82 (30)
Na	0.0048 (2)	0.0018 (2)	0.0020 (1)	0.018 (2)	0.0037 (24)	0.0020 (0)	0.27 (2)	0.0028 (4)	0.018 (3)	0.28 (1)	0.63 (0)
Rb	0.012 (11)	-	-	0.008 (5)	0.0018 (8)	-	-	-	-	-	-
Sr	0.007 (4)	0.00011 (8)	-	0.0018 (9)	0.006 (4)	0.0021 (14)	0.23 (12)	0.0028 (19)	0.0034 (23)	0.21 (3)	0.26 (7)
Ca	0.012 (3)	0.005 (2)	0.016 (8)	0.58 (24)	0.049 (39)	0.96 (73)	19 (13)	0.025 (11)	0.78 (34)	20 (8)	7 (3)
Mg	3.30 (38)	9 (3)	38 (9)	24 (6)	81 (37)	51 (23)	24 (11)	122 (93)	77 (59)	34 (26)	39 (30)
Mn	0.46 (8)	0.78 (28)	1.17 (57)	4 (2)	2 (1)	4 (2)	4 (2)	1.4 (1)	4.1 (1)	5.2 (5)	3.82 (22)
Fe	13 (4)	7 (4)	15 (7)	32 (14)	6 (1)	10 (2)	13 (2)	32 (9)	60 (15)	92 (23)	109 (26)
Ni	113 (32)	45 (27)	113 (71)	50 (32)	243 (113)	94 (44)	52 (24)	175 (15)	80 (7)	58 (5)	120 (23)
B	0.022 (6)	0.085 (59)	0.83 (46)	0.8 (4)	0.073 (16)	-	-	0.50 (10)	-	-	0.58 (10)
Al	0.0045 (24)	0.004 (1)	0.015 (7)	0.86 (25)	0.10 (6)	4 (2)	14 (8)	0.053 (26)	3 (2)	10 (5)	35 (17)
Cr	0.75 (8)	1.75 (81)	12 (4)	4 (1)	5 (4)	24 (15)	6.5 (5)	21 (6)	15 (5)	2.71 (80)	2 (1)
Sc	0.13 (2)	0.28 (11)	1.38 (54)	23 (6)	9 (5)	76 (38)	427 (283)	-	-	-	-
La	-	-	-	-	-	-	0.77 (34)	-	-	0.56 (35)	0.93 (66)
Ce	0.0078 (40)	-	0.022 (15)	0.015 (9)	0.012 (9)	-	0.96 (62)	0.016 (11)	-	1.06 (38)	1.76 (77)
Pr	-	-	-	-	-	-	2 (1)	-	-	1.82 (84)	2.11 (93)
Nd	-	-	-	-	-	-	3 (2)	-	-	4 (2)	4 (2)
Lu	0.017 (4)	0.017 (6)	0.043 (23)	1.3 (6)	0.25 (17)	4 (3)	41 (29)	0.20 (8)	8 (3)	80 (30)	37 (14)
Y	-	-	-	0.41 (19)	-	0.27 (22)	6 (3)	-	0.54 (26)	16 (5)	6 (2)
Ti	0.009 (3)	0.009 (3)	0.022 (6)	0.51 (12)	0.17 (8)	4 (2)	14 (6)	0.14 (5)	4 (1)	4 (1)	12 (4)
Zr	-	-	-	0.042 (26)	-	-	-	-	-	15 (10)	36 (19)
V	0.0019 (4)	0.0018 (7)	0.0083 (36)	0.039 (17)	0.014 (14)	0.073 (65)	-	0.046 (27)	0.22 (12)	0.86 (14)	7 (1)
P	0.12 (2)	0.09 (3)	0.23 (10)	0.22 (10)	0.23 (5)	0.28 (7)	0.27 (7)	0.21 (9)	0.35 (17)	0.33 (14)	0.29 (12)
Nb	0.009 (3)	-	-	-	-	-	-	-	-	-	9 (4)
Ta	0.0086 (23)	-	0.08 (4)	-	-	-	-	-	-	-	-

occurred. At 1,200 °C, forsterite has a F content of 900 ± 40 ppm and a Cl content of 170 ± 70 ppm. Enstatite shows a Cl content of 30 ± 20 ppm, similar to the opx in the run with natural starting composition. The aqueous fluids are homogeneous with respect to their major element composition. Most trace elements were below detection limit both in minerals and in the quenched solute. Concentrations measured with LA-ICP-MS and calculated partition coefficients (mineral/fluid) are illustrated in Fig. 3 and listed in the Online Resource 1 and in Table 3.

Fluid compositions

The compositions of the aqueous fluids were determined with LA-ICP-MS (Online Resource 1). The aqueous fluids of each run are homogenous with respect to their major element composition and contain large amount of silicate components (mainly Si, Mg, Al, Ca, Na and Cl). Measured fluid compositions are generally consistent from run to run with the temperature of the run.

The plot of the MgO/SiO₂ molar ratios of the fluids versus the temperature of the runs (Fig. 4) shows a positive correlation, probably reflecting a decreased solubility of silica with temperature.

Mineral/fluid partition coefficients

Mineral/fluid partition coefficients (Fig. 3) show that Cl and the large ionic lithophile elements (LILE) always partition into the fluid phase, whereas most other trace elements behave compatible in clinopyroxene and amphibole, moderately incompatible to compatible in orthopyroxene and incompatible in olivine (Fig. 3). These findings, specifically the order $D^{\text{amph}/\text{fluid}} \approx D^{\text{cpx}/\text{fluid}} > D^{\text{opx}/\text{fluid}} > D^{\text{ol}/\text{fluid}}$, is in general agreement with previous studies (Mysen 1979; Brenan et al. 1995; Ayers et al. 1997; Stalder et al. 1998; Caciagli et al. 2011; Fabbri et al. 2013). In contrast, $D^{\text{mineral}/\text{fluid}}$ is very similar for Li and P for all observed silicate phases.

Measured olivine/fluid partition coefficients show that olivine strongly depletes Cl, Na, Ce and Sr relative to the fluid (Fig. 3), with low values for Cl $\sim 10^{-4}$, intermediate values for Na and Sr ($\sim 10^{-3}$) and higher values for Ce ($\sim 10^{-2}$). Olivine/fluid values for Li, B, Ti, Lu, V and P are $\sim 10^{-1}$.

Orthopyroxene/fluid values (Fig. 3) are given as follows: Cl $\sim 10^{-4}$, Sr $\sim 10^{-3}$, Na and Ce $\sim 10^{-2}$, Li, Y, V and P $\sim 10^{-1}$, Ti and Lu ~ 5 .

Clinopyroxene/fluid partition coefficients show a strong enrichment of Pr, Nd, Zr, Ti, Y and Lu in clinopyroxene relative to the fluid (Fig. 3), with values for Lu $\sim 10^2$, for Ti, Y, Nd, Pr and Zr in the range 1–10. Clinopyroxene/fluid

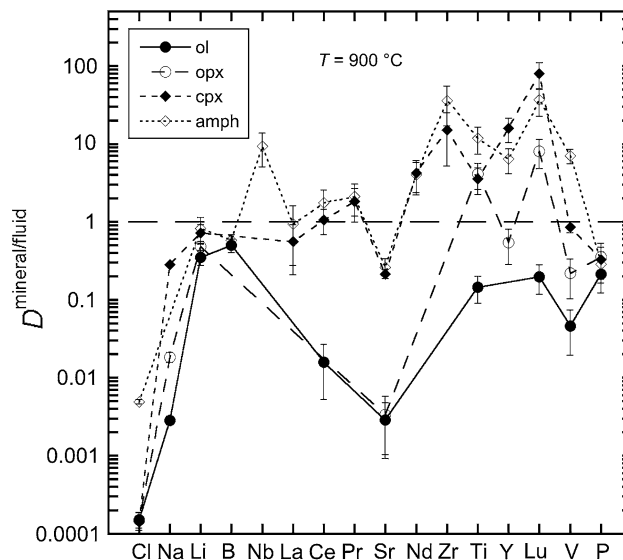


Fig. 3 Representative mineral/fluid partition coefficients for coexisting minerals from experiments Cl-26. The horizontal dashed line represent the limit between compatibility ($D^{\text{mineral}/\text{fluid}} > 1$) and incompatibility ($D^{\text{mineral}/\text{fluid}} < 1$)

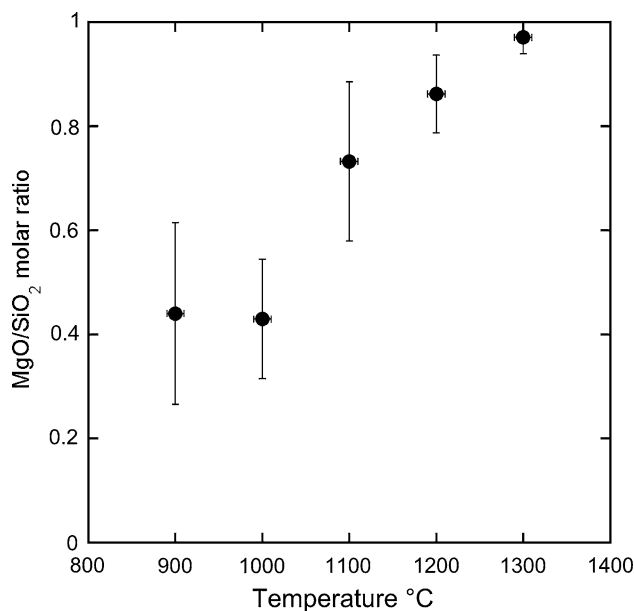


Fig. 4 MgO/SiO₂ molar ratio of the fluids calculated from the LA-ICP-MS analyses (Online Resource 1) versus the temperature (°C) of the runs

values for Na, Li, La, Sr, V and P are in the range 10^{-1} –1 and for Cl are $\sim 10^{-4}$.

Amphibole is enriched in Nb, Ce, Pr, Nd, Zr, Ti, Y, Lu and V with respect to the fluid with amphibole/fluid values larger than 1 (Fig. 3). Amphibole/fluid values are in the range $\sim 10^{-1}$ –1 for Li, B, La, Sr, P and $\sim 5 \times 10^{-3}$ for Cl.

One important factor controlling olivine-fluid trace element partitioning is the solute content of the fluid phase (Fig. 5). As observed in previous studies (Stalder et al. 2001; Kessel et al. 2004), the total solute content is positively correlated with temperature (Online Resource 1) concomitant with a decrease in $D^{\text{ol/fluid}}$. This trend is extremely pronounced for some cations (e.g., Ti), with $D^{\text{ol/fluid}}$ dropping by 1–2 log units as the solute content increases to a similar extent. Similar effects on $D^{\text{mineral/fluid}}$ were reported by Brenan and Watson (1991) and Brenan et al. (1995).

Cl and F partition coefficients

Cl mineral/fluid partition coefficients (D_{Cl}) were calculated from the Cl concentration in the mineral measured by EMPA and the Cl concentration of the coexisting fluid measured by LA-ICP-MS. The $D_{\text{Cl}}^{\text{ol/fl}}$ is between 9×10^{-5} and 2×10^{-4} . Chlorine in orthopyroxene is more compatible than in olivine with $D_{\text{Cl}}^{\text{opx/fl}}$ values between 1.5×10^{-4} and 3.7×10^{-4} . Clinopyroxene has $D_{\text{Cl}}^{\text{cpx/fl}}$ values of 1.4×10^{-4} and 2×10^{-4} similar to orthopyroxene, and amphibole shows the highest $D_{\text{Cl}}^{\text{amph/fl}}$ value of 4.9×10^{-3} . For fluorine and for runs performed without diamond trap, the partition coefficients can be estimated as the ratio between the concentration in mineral versus the concentration in the starting mixture. We obtain $D_{\text{F}}^{\text{fo/startmix}} \sim 0.1$ for forsterite characterized by the presence of humite-type point defects, $D_{\text{F}}^{\text{hu/startmix}} = 6.25$ and $D_{\text{F}}^{\text{di/startmix}} = 0.14$ for diopsidic pyroxene (Table 2). The values for $D_{\text{Cl}}^{\text{ol/startmix}}$ are between 1.6×10^{-3} and 5.3×10^{-4} and that for $D_{\text{Cl}}^{\text{opx/startmix}}$ vary between 1.8×10^{-4} and 3.2×10^{-4} in close agreement with the calculated partition coefficients.

IR spectra and IR images

Unpolarized IR spectra collected on olivine are shown in Fig. 6, and IR images that were recorded for visualization of the OH defects on the entire experimental charge are shown in Fig. 7.

Ti-bearing olivine crystals (Online Resource 1, Fig. 6), synthesized using the natural peridotite as starting material, exhibit absorption bands at 3,326, 3,354, 3,525, 3,571 and 3,612 cm^{-1} . Olivine from the natural F-doped peridotite (Table 2; Fig. 6) displays also the absorption band at 3,535, 3,595, 3,640 and 3,670 cm^{-1} , and the band at 3,570 cm^{-1} tends to become stronger (i.e., higher intensity). Olivine crystallized under relatively oxidizing conditions ($f\text{O}_2 = \text{QFM} + 1.5$) shows an IR spectrum similar to that of olivine crystallized with no constrain on $f\text{O}_2$, whereas the IR spectra of olivine crystallized under

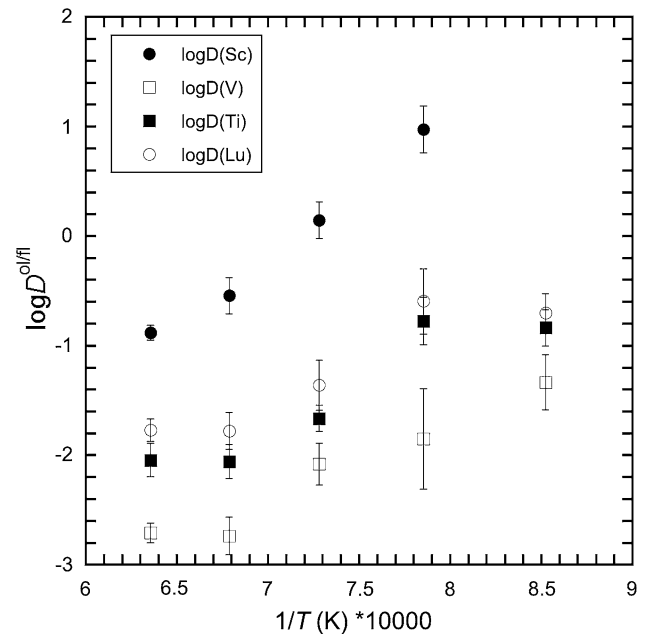


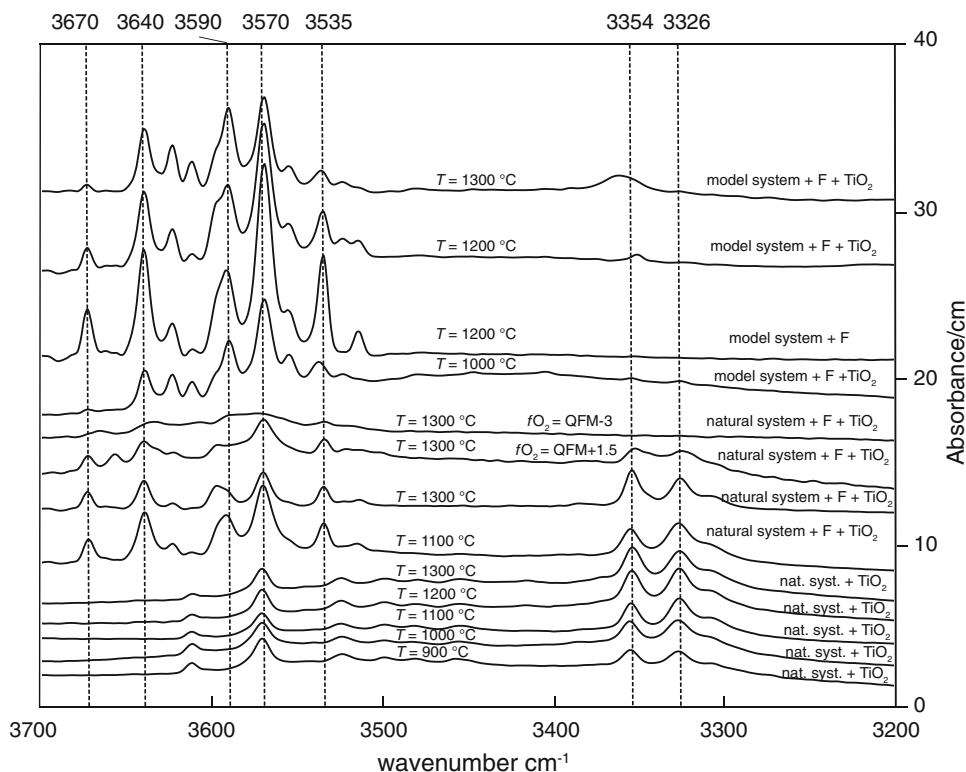
Fig. 5 Partition coefficients $\log D^{\text{ol/fluid}}$ for some trace elements as function of the inverse temperature (K)

reducing conditions ($f\text{O}_2 = \text{QFM} - 3$) do not have bands at 3,326 and 3,354 cm^{-1} and those over 3,500 cm^{-1} tend to be less intense. This observation supports the idea that the bands around 3,350 cm^{-1} can be assigned to Fe^{3+} -related OH defects (Berry et al. 2007) and that olivine grown at low $f\text{O}_2$ (below the Fe–FeO) contains much less water with respect to crystals from relatively more oxidized experiments (Grant et al. 2007b). Forsterite from the F-bearing model system (Table 2; Fig. 6) displays the strongest absorption bands at wavenumber similar to those for olivine from the natural peridotite plus F system. The main absorption bands are located at 3,569 and 3,536 cm^{-1} , and the bands above 3,590 cm^{-1} are more intense with respect to the bands for olivine from the F-doped natural peridotite system. In addition, the bands at 3,326 and 3,354 cm^{-1} are absent. The thickness of the samples is comparable, and hence, the intensity of absorption is related to the amount of OH. The observed spectra indicate that the presence of F in the system permits to incorporate much more OH in olivine compared with olivine from the Ti-bearing and F-free system.

IR images (Fig. 7) were recorded on the whole sample Cl–F-1 containing the fluorine-rich forsterite crystals (Table 2; Fig. 6). No absorption bands close to 3,400 cm^{-1} were detected, suggesting the absence or a very low abundance of humite-type planar defects (Hermann et al. 2007).

Additional data on the amounts of water dissolved in olivine are reported in the Online Resource 2.

Fig. 6 Unpolarized IR spectra of olivine averaged over 10–15 randomly oriented crystals for each run. Spectra are normalized to 1 cm thickness. Vertical dashed lines indicate the positions of OH bands. Experimental run details are labeled above each spectrum



TEM

The analyzed TEM foils were cut from a forsterite crystal from sample Cl-F-1 with orientation $\sim [714]$ as determined by EBSD. This sample was chosen due to the high fluorine content of its forsterite (Table 2). The foils were cut after chemical polishing of the sample. Chemical polishing results in preferential material removal in regions with defects. Lamellar features that are approximately oriented in the direction expected for humite-type defects (parallel $(001)_{\text{Ol}}$) are observed in the BSE image (Fig. 8a). Three TEM foils were cut, two across these features and one parallel, in order to determine its origin. Neither bright field TEM, nor HRTEM or STEM did show any chemical or structural variations in the investigated foils. As far as planar defects such as humite-lamellae are concerned, selected area diffraction in $[100]$, $[110]$ or $[010]$ should depict evidence in the form of streaks, as humite has significantly different lattice parameters to olivine, always assuming the presence of enough such lamellae. The streaks in the diffraction pattern would be perpendicular to the plane of their orientation. Thus, the effect should best be visible on (001) diffraction spots, examples are given in Hermann et al. (2007), Kitamura et al. (1987), Risold et al. (2001), and Wirth et al. (2001). No such streaks were observed. Instead of lamellae, dislocations were observed in the bright field image (Fig. 8b), indicating another type of

defect hitherto not considered as potential repository for halogens and hydrogen. However, the absence of planar defects cannot be proved, but the concentration is certainly rather low in this sample. Considering the fluorine content of the analyzed forsterite (0.09 wt% F) and the ideal fluorine content in stoichiometric F-clinohumite (6.1 wt% F), the hypothetical fraction of F-clinohumite hosted in the forsterite lattice is approximately 1.5%, corresponding to 0.34 mol% clinohumite in forsterite. For TEM observations, this would mean that only 1 out of 300 d-spacing perpendicular to the lamellae would appear broader.

Discussion

Halogen partitioning and major hosts for halogens in the mantle

Our single data point from experiment crystallizing forsterite with clinohumite defects gives $D_{\text{Ol}}^{\text{F/Cl}} = 5.3$, in agreement with the general observation that F is less incompatible than Cl in olivine (e.g., $D_{\text{Ol}}^{\text{F/Cl}}$ values between 0.9 and 13 Hauri et al. 2006; Beyer et al. 2012; Dalou et al. 2012). Our results for chlorine partitioning between mantle minerals and coexisting aqueous fluid (Table 3) are in good agreement with results from the system forsterite–enstatite–pyrope– H_2O – MgCl_2 at 1,100 °C and 2.6 GPa (Bernini

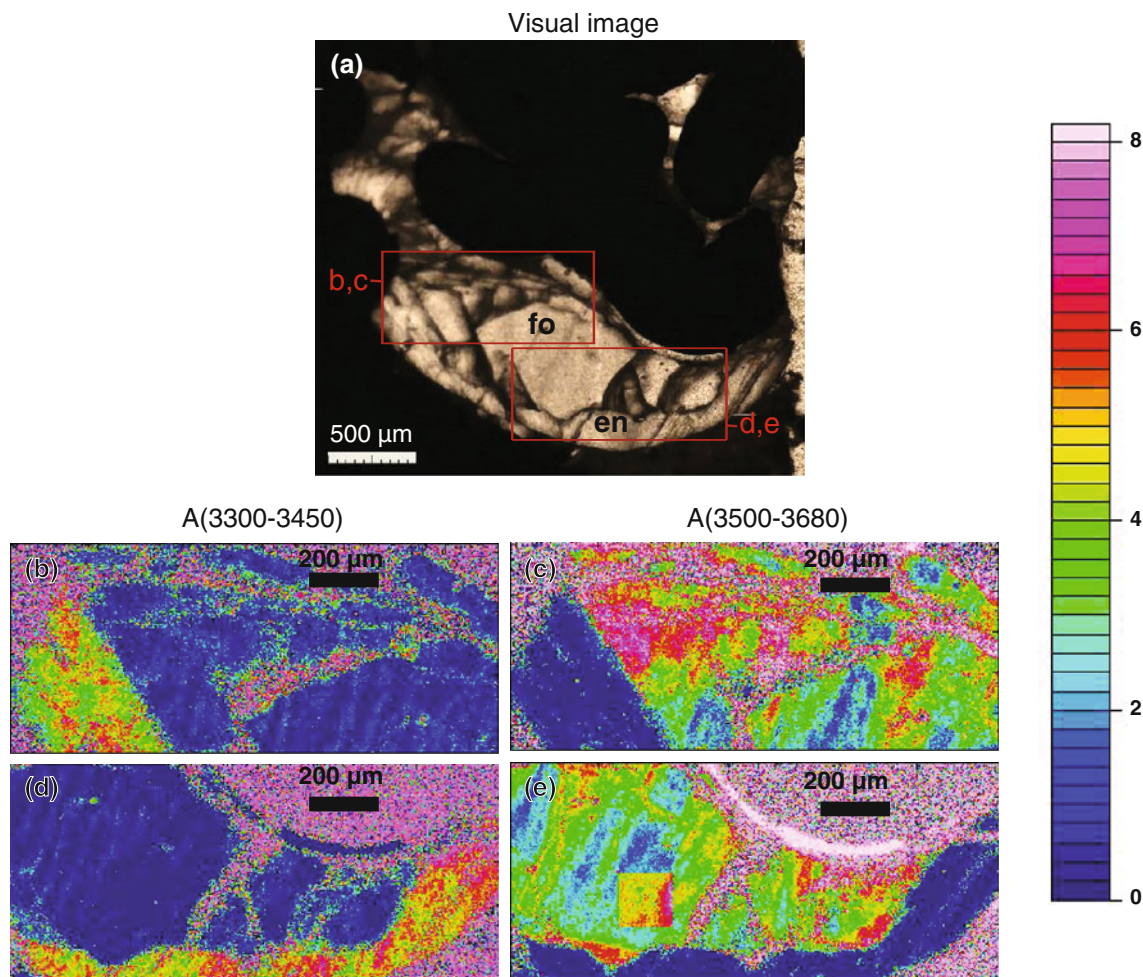


Fig. 7 Visual image **a** of sample Cl-F-1, **b–e** IR images displaying total absorbances in the wavenumber range (see *color code* right) **b**, **d** 3,300–3,450 cm^{-1} and **c**, **e** 3,500–3,680 cm^{-1} *color-coded* according to the *scale bar* to the right (not normalized to thickness). Each pixel ($2.7 \times 2.7 \mu\text{m}^2$) contains the full information of an IR spectrum and can be extracted separately. Note the absence of any band close to

3,400 cm^{-1} indicating the absence of humite-type planar defects (Hermann et al. 2007). The *rectangular* feature left to the *center* in (e) represents one $170 \times 170 \mu\text{m}^2$ frame. Compared to the surrounding frames, it exhibits enhanced absorbance interpreted as analytical artifact probably caused by an electric spike during data acquisition

et al. 2013) and with those from the system $\text{MgO-SiO}_2\text{-H}_2\text{O-NaCl} \pm \text{TiO}_2 \pm \text{Al}_2\text{O}_3$ at 900–1,300 °C and 2 GPa (Fabrizio et al. 2013) having partition coefficients for $D_{\text{Cl}}^{\text{fo/fl}}$ and for $D_{\text{Cl}}^{\text{en/fl}}$ between 10^{-5} and 10^{-3} .

The observed Cl concentrations in olivine crystals from this study are similar to the Cl content of olivine from high-pressure serpentinite and from metamorphic harzburgite, where Cl concentrations of 24–120 and 7–18 ppm, respectively, were detected (Scambelluri et al. 2004). Chlorine concentrations in natural olivine from spinel peridotites and oceanic basalts are lower and fairly homogeneous at 5.7 ± 0.5 ppm (Beyer et al. 2012). An implication of the present work is that halogens in the mantle may be incorporated in olivine as well as in other nominally anhydrous minerals (for example, pyroxenes) in addition to hydrous minerals such as amphibole, serpentine

or chlorite. Taking into account the modal proportions in the mantle and estimations for the total halogen content (Saal et al. 2002), olivine may be regarded as an important host for halogens in the Earth's mantle.

Incorporation mechanism of halogens into nominally halogen-free minerals

In analogy to OH incorporation in olivine, two different groups of defects can be encountered for halogen incorporation in olivine: point defects (Berry et al. 2005, 2007) and planar defects (Kitamura et al. 1987; Hermann et al. 2007). Both groups of defects permit to incorporate OH in the forsterite structure and thus can serve as host for halogens by permitting a direct exchange between halogens and OH. Planar defects are more likely close to the clinohumite

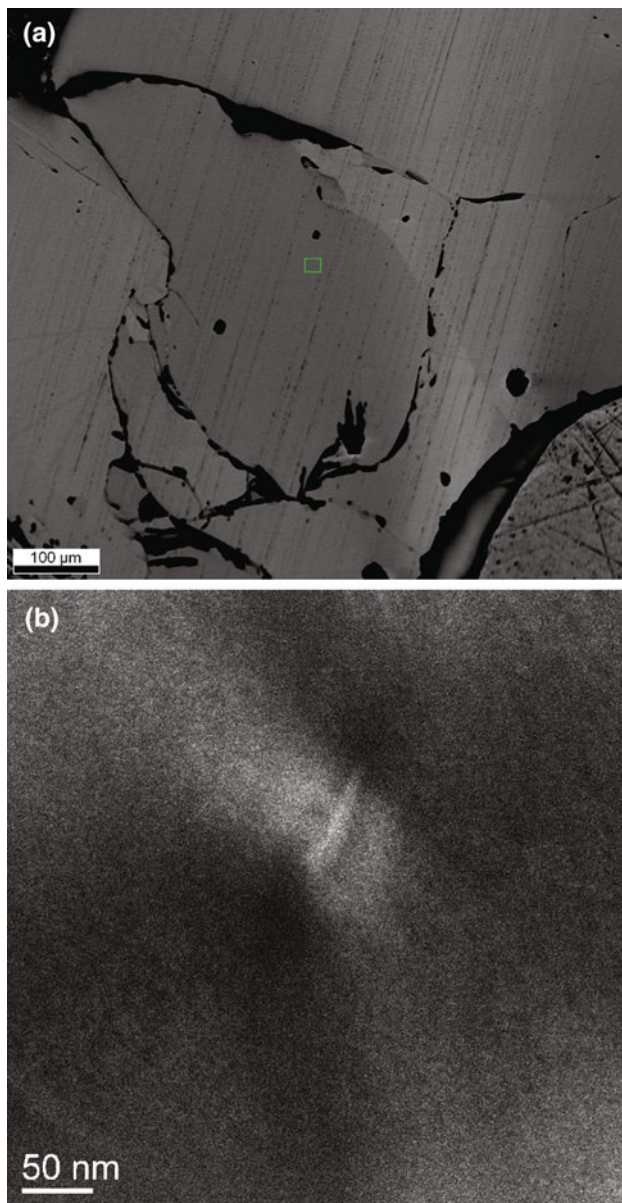


Fig. 8 **a** Backscattered electron image of sample CL-F-1 showing lamellar features in the olivine crystals. The *rectangle* in the center depicts one of the regions from where EBSD measurements were taken. **b** Bright field image showing a dislocation in the olivine crystal

breakdown curve that depends on the P – T – X conditions (Weiss 1997; Ulmer and Trommsdorff 1999), but at conditions far above the clinohumite breakdown, OH and halogen incorporation is dominated by point defects (Hermann et al. 2007). Olivine IR absorption bands have been related to the type of defect permitting thus to distinguish between point and planar defects. IR absorption bands at 3,525 and 3,572 cm^{-1} have been assigned to humite-type point defects (Berry et al. 2005), whereas band at $\sim 3,400 \text{ cm}^{-1}$ is related to humite-type planar defects (Hermann et al. 2007). IR spectra recorded on F \pm Ti-bearing olivine (Fig. 6) reveal

strong absorption bands at 3,535 and $\sim 3,570 \text{ cm}^{-1}$, and no absorption band close to $3,400 \text{ cm}^{-1}$ is revealed in the IR spectra of the same crystals and in the IR images (Fig. 7) of the fluorine-rich forsterite investigated by TEM, suggesting the presence of humite-type point defects instead of humite-type planar defects. Note that the bands at 3,535 and $\sim 3,570 \text{ cm}^{-1}$ tend to be less intense for F-free Ti-bearing olivine and for olivine coexisting with F-bearing minerals, whereas they tend to become more intense in the F-bearing systems at lower temperature. These observations suggest that in the F–Ti-bearing system, lower temperatures tend to promote the stabilization of point defects in olivine. In the olivine crystal investigated by TEM, no indications for humite-lamellae were found. This observation is in accord with the IR spectrum and images recorded on the same crystal, where no absorption bands around $3,400 \text{ cm}^{-1}$ were detected, and—considering the relatively high synthesis temperature of 1,200 $^{\circ}\text{C}$ —the predominance of point defects was actually expected (Hermann et al. 2007). However, the observation of a dislocation may suggest that the concept of different defect regimes in the P – T – X -space is more complex than previously elaborated. It may be speculated that between the regimes of planar defects (at temperatures just above the clinohumite breakdown, Hermann et al. 2007) and point defects (far above clinohumite breakdown), a defect regime where dislocations prevail may exist.

Acknowledgments This project was supported with a Lise Meitner grant to A.F. by the Austrian Science Fund (FWF): [M1266-N21]. We thank Martina Tribus for her assistance with electron microprobe analyses and Hannes Witting and Fabian Höpferger from the mechanical workshop for manufacturing the high-pressure assemblies for the experiments. Richard Tessadri is thanked for performing the XRD analysis. We thank two anonymous reviewers for constructive comments.

Open Access This article is distributed under the terms of the Creative Commons Attribution License which permits any use, distribution, and reproduction in any medium, provided the original author(s) and the source are credited.

References

- Aerts M, Hack AC, Reusser E, Ulmer P (2010) Assessment of the diamond-trap method for studying high-pressure fluids and melts and an improved freezing stage design for laser ablation ICP-MS analysis. *Am Mineral* 95:1523–1526
- Aiuppa A, Baker DR, Webster JD (2009) Halogens in volcanic systems. *Chem Geol* 263:1–18
- Aranovich LY, Newton RC (1996) H_2O activity in concentrated NaCl solutions at high pressures and temperatures measured by the brucite-periclase equilibrium. *Contrib Mineral Petrol* 125:200–212
- Aranovich LY, Newton RC (1997) H_2O activity in concentrated KCl and KCl–NaCl solutions at high pressures and temperatures

- measured by the brucite-periclase equilibrium. *Contrib Mineral Petrol* 127:261–271
- Ayers JC, Dittmer SK, Layne GD (1997) Partitioning of elements between peridotite and H₂O at 2.0–3.0 GPa and 900–1100 °C, and application to models of subduction zone processes. *Earth Planet Sci Lett* 150:381–398
- Baker DR, Balcone-Boissard E (2009) Halogen diffusion in magmatic systems: our current state of knowledge. *Chem Geol* 263:82–88
- Bell DR, Rossman GR (1992) Water in Earth's mantle the role of nominally anhydrous minerals. *Science* 255:1391–1397
- Bernini D, Wiedenbeck M, Dolejš D, Keppler H (2013) Partitioning of halogens between mantle minerals and aqueous fluids: implications for the fluid flow regime in subduction zones. *Contrib Mineral Petrol* 165:117–128
- Berry AJ, Hermann J, O'Neill HSC, Foran GJ (2005) Fingerprinting the water site in mantle olivine. *Geology* 33:869–872
- Berry AJ, O'Neill HSC, Hermann J, Scott DR (2007) The infrared signature of water associated with trivalent cations in olivine. *Earth Planet Sci Lett* 261:134–142
- Beyer C, Klemme S, Wiedenbeck M, Stracke A, Vollmer C (2012) Fluorine in nominally fluorine-free mantle minerals: experimental partitioning of F between olivine, orthopyroxene and silicate melts with implications for magmatic processes. *Earth Planet Sci Lett* 337–338:1–9
- Brenan JM, Watson EB (1991) Partitioning of trace elements between olivine and aqueous fluids at high *P-T* conditions: implications for the effect of fluid composition on trace elements transport. *Earth Planet Sci Lett* 107:672–688
- Brenan JM, Shaw HF, Ryerson FJ, Phinney DL (1995) Mineral-aqueous fluid partitioning of trace elements at 900 °C and 2.0 GPa: constraints on the trace element chemistry of mantle and deep crustal fluids. *Geochim Cosmochim Acta* 59:3331–3350
- Bromiley DW, Kohn SC (2007) Comparisons between fluoride and hydroxide incorporation in nominally anhydrous and fluorine-free mantle minerals. *Geochim Cosmochim Acta* 71:A124
- Caciagli N, Brenan JM, McDonough WF, Phinney D (2011) Mineral-fluid partitioning of lithium and implications for slab-mantle interaction. *Chem Geol* 280:384–398
- Carroll MR, Webster JD (1994) Solubilities of sulfur, noble gases, nitrogen, chlorine, and fluorine in magmas. *Rev Mineral Geochem* 30:231–279
- Chu L, Enggist A, Luth RW (2011) Effect of KCl on melting in the Mg₂SiO₄–MgSiO₃–H₂O system at 5 GPa. *Contrib Mineral Petrol* 162:565–571
- Dalou C, Koga KT, Shimizu N, Boulon J, Devidal J (2012) Experimental determination of F and Cl partitioning between lherzolite and basaltic melt. *Contrib Mineral Petrol* 163:591–609
- Drury MR (1991) Hydration-induced climb dissociation of dislocations in naturally deformed mantle olivine. *Phys Chem Miner* 18:106–116
- Fabbrizio A, Stalder R, Hametner K, Günther D (2013) Experimental chlorine partitioning between forsterite, enstatite and aqueous fluid at upper mantle conditions. *Geochim Cosmochim Acta*. doi:10.1016/j.gca.2013.05.026
- Giannuzzi LA, Drown JL, Brown SR, Irwin RB, Stevie FA (1997) Focused ion beam milling and micromanipulation lift-out for site-specific cross-section TEM specimen preparation. In: Anderson R, Walck S (eds) *Proceedings of the Materials Research Society: workshop on specimen preparation for TEM of materials IV*, vol 480. Materials Research Society, Pittsburgh, pp 19–27
- Grant K, Brooker RA, Kohn SC, Wood BJ (2007a) The effect of oxygen fugacity on hydroxyl concentrations and speciation in olivine: implications for water solubility in the upper mantle. *Earth Planet Sci Lett* 261:217–229
- Grant K, Ingrin J, Lorand JP, Dumas P (2007b) Water partitioning between mantle minerals from peridotite xenoliths. *Contrib Mineral Petrol* 154:15–34
- Günther D, Frischknecht R, Heinrich C, Kahlert H (1997) Capabilities of an argon fluoride 193 nm excimer laser for laser ablation inductively coupled plasma mass spectrometry microanalysis of geological materials. *J Anal Atom Spectrom* 12:939–944
- Hauri EH, Gaetani GA, Green TH (2006) Partitioning of water during melting of the Earth's upper mantle at H₂O-undersaturated conditions. *Earth Planet Sci Lett* 248:715–734
- Hermann J, Fitz Gerald JD, Malaspina N, Berry AJ, Scambelluri M (2007) OH-bearing planar defects in olivine produced by the breakdown of Ti-rich humite minerals from Dabie Shan (China). *Contrib Mineral Petrol* 153:417–428
- Hirschmann MM, Aubaud C, Withers AC (2005) Storage capacity of H₂O in nominally anhydrous minerals in the upper mantle. *Earth Planet Sci Lett* 236:167–181
- Hirth G, Kohlstedt DL (1996) Water in the oceanic upper mantle: implications for rheology, melt extraction and the evolution of the lithosphere. *Earth Planet Sci Lett* 144:93–108
- Karato S, Jung H (1998) Water, partial melting and the origin of the seismic low velocity zone in the upper mantle. *Earth Planet Sci Lett* 157:193–207
- Kessel R, Ulmer P, Pettke T, Schmidt MW, Thompson AB (2004) A novel approach to determine high-pressure high-temperature fluid and melt compositions using diamond-trap experiments. *Am Mineral* 89:1078–1086
- Kitamura M, Kondoh S, Morimoto N, Miller GH, Rossman GR, Putnis A (1987) Planar OH-bearing defects in mantle olivine. *Nature* 328:143–145
- Kushiro I, Yoder HS (1969) Melting of forsterite and enstatite at high pressures under hydrous conditions. *Carnegie Inst Wash Year B* 67:153–158
- Lee MR, Bland PA, Graham G (2003) Preparation of TEM samples by focused ion beam (FIB) techniques; applications to the study of clays and phyllosilicates in meteorites. *Mineral Mag* 67:581–592
- Mysen BO (1979) Trace element partitioning between garnet peridotite minerals and water-rich vapor: experimental data from 5 to 30 kbar. *Am Mineral* 64:274–287
- O'Neill HSC (1988) Systems Fe–O and Cu–O: thermodynamic data for the equilibria of Fe–“FeO”, Fe–Fe₃O₄, “FeO”–Fe₃O₄, Fe₃O₄–Fe₂O₃, Cu–Cu₂O and Cu₂O–CuO from emf measurements. *Am Mineral* 73:470–487
- O'Neill HSC, Pownceby MI (1993) Thermodynamic data from redox reactions at high temperatures. 1. An experimental and theoretical assessment of the electrochemical method using stabilized zirconia electrolytes, with revised values for the Fe–FeO, Co–CoO, Ni–NiO and Cu–Cu₂O oxygen buffers, and new data from the W–WO₂ buffer. *Contrib Mineral Petrol* 114:296–314
- Oehm J, Schneider A, Wedepohl KH (1983) Upper mantle rocks from basalts of the northern Hessian depression (NW Germany). *Tschermaks Min Petr Mitt* 32:25–48
- Phaneuf MW (1999) Applications of focused ion beam microscopy to materials science specimens. *Micron* 30:277–288
- Rauch M, Keppler H (2002) Water solubility in orthopyroxene. *Contrib Mineral Petrol* 143:525–536
- Reed MH (1997) Hydrothermal alteration and its relationship to ore fluid composition. In: Barnes HL (ed) *Geochemistry of hydrothermal ore deposits*, 3rd edn. Wiley, New York, pp 303–366
- Risold AC, Trommsdorff V, Grobety B (2001) Genesis of ilmenite rods and palisades along humite-type defects in olivine from Alpe Arami. *Contrib Mineral Petrol* 140:619–628
- Saal AE, Hauri EH, Langmuir CH, Perfit MR (2002) Vapour under saturation in primitive mid-ocean-ridge basalt and the volatile content of Earth's upper mantle. *Nature* 419:451–455

- Scambelluri M, Münthener O, Ottolini L, Pettke T, Vannucci R (2004) The fate of B, Cl and Li in the subducted oceanic mantle and in the antigorite breakdown fluids. *Earth Planet Sci Lett* 222:217–234
- Shmulovich KI, Graham CM (1996) Melting of albite and dehydration of brucite in H_2O –NaCl fluids to 9 kbars and 700–900 °C: implications for partial melting and water activities during high pressure metamorphism. *Contrib Mineral Petrol* 124:370–382
- Stalder R, Ulmer P (2001) Phase relations of a serpentine composition between 5 and 14 GPa: significance of clinohumite and phase E as water carriers into the transition zone. *Contrib Mineral Petrol* 140:670–679
- Stalder R, Foley SF, Brey GP, Horn I (1998) Mineral–aqueous fluid partitioning of trace elements at 900–1,200 °C and 3.0–5.7 GPa: new experimental data for garnet, clinopyroxene and rutile, and implications for mantle metasomatism. *Geochim Cosmochim Acta* 62:1781–1801
- Stalder R, Ulmer P, Thompson AB, Günther D (2001) High pressure fluids in the system MgO – SiO_2 – H_2O under upper mantle conditions. *Contrib Mineral Petrol* 140:607–618
- Stalder R, Klemme S, Ludwig T, Skogby H (2005) Hydrogen incorporation in orthopyroxene: interaction of different trivalent cations. *Contrib Mineral Petrol* 150:473–485
- Stalder R, Kronz A, Simon K (2008) Hydrogen incorporation in enstatite in the system MgO – SiO_2 – H_2O –NaCl. *Contrib Mineral Petrol* 156:653–659
- Tenner TJ, Hirschmann MM, Withers AC, Hervig RL (2009) Hydrogen partitioning between nominally anhydrous upper mantle minerals and melt between 3 and 5 GPa and applications to hydrous peridotite partial melting. *Chem Geol* 262:42–56
- Ulmer P, Trommsdorff V (1999) Phase relations of hydrous mantle subducting to 300 km. In: Fei Y, Berthka CM, Mysen B (eds) *Mantle petrology: field observations and high pressure experimentation: a tribute to Francis R. (Joe) Boyd*. The Geochemical Society, Special publication No. 6, pp 259–281
- Vignerresse JL (2009) Evaluation of the chemical reactivity of the fluid phase through hard–soft acid–base concepts in magmatic intrusions with applications to ore generation. *Chem Geol* 263:69–81
- Webster JD, Sintoni MF, De Vivo B (2009) The partitioning behavior of Cl, S and H_2O in aqueous vapor- ± saline liquid saturated phonolitic and trachytic melts at 200 MPa. *Chem Geol* 263: 19–63
- Weiss M (1997) Clinohumites: a field and experimental study. Dissertation, ETH-Zürich
- Wirth R (2004) Focused ion beam (FIB): a novel technology for advanced application of micro- and nanoanalysis in geosciences and applied mineralogy. *Eur J Mineral* 16:863–876
- Wirth R, Dobrzhinetskaya L, Green HW II (2001) Electron microscope study of the reaction $olivine + H_2O + TiO_2 = titanian clinohumite + titanian chondrodite$ synthesized at 8 GPa, 1,300 K. *Am Mineral* 86:601–610
- Yardley BWD (2005) Metal concentrations in crustal fluids and their relationship to ore formation. *Econ Geol* 100:613–632